Research Article | Vol. 27, No. 11 | 27 May 2019 | OPTICS EXPRESS 16121
Optics EXPRESS

1 m long multilayer-coated deformable piezoelectric bimorph mirror for adjustable focusing of high-energy X-rays

JOHN P. SUTTER,[1,*] PHILIP A. CHATER,[1] RICCARDO SIGNORATO,[2] DEAN S. KEEBLE,[1] MICHAEL R. HILLMAN,[1] MATTHEW G. TUCKER,[1] SIMON G. ALCOCK,[1] IOANA-THEODORA NISTEA,[1] AND HERIBERT WILHELM[1,3]

[1]*Diamond Light Source Ltd, Chilton, Didcot, Oxfordshire, OX11 0DE, UK*

[2]*CINEL Strumenti Scientifici s.r.l. via dell'Artigianato, 14-14/A, 35010 Vigonza (Padova), Italy & S. RI. Tech s.r.l.s., viale del lavoro, 42A, 35010 Vigonza (Padova), Italy*

[3]*Helmholtz Institut Ulm, Helmholtzstraße 11, D-89081 Ulm, Germany*
**john.sutter@diamond.ac.uk*

Abstract: The Diamond Light Source (DLS) beamline I15-1 measures atomic pair distribution functions (PDF) using scattering of 40-80 keV X-rays. A unique focusing element was needed to condense these X-rays from an initial large cross section (11.0 mm H × 4.2 mm V) into a required spot size of FWHM ≈680 μm (H) × 20 μm (V) at a variable position between the sample and the detector. The large numerical aperture is achieved by coating a silicon substrate over 1 m long with three multilayer stripes of Bragg angle 4.2 mrad. One stripe selects X-rays of each energy 40.0, 65.4, and 76.6 keV. Sixteen piezoelectric bimorph actuators attached to the sides of the mirror substrate adjusted the reflecting surface's shape. Focal spots of vertical width < 15 μm were obtained at three positions over a 0.92 m range, with fast, easy switching from one focal position to another. Minimized root mean square slope errors were close to 0.5 μrad after subtraction of a uniform curvature. Reflectivity curves taken along each stripe showed consistent high peaks with generally small angular variation of peak positions. This is the first application of a 1 m long multilayer-coated bimorph mirror at a synchrotron beamline. Data collected with its help on a slice of a lithium ion battery's cathode are presented.

1. Introduction

1.1 Requirements for quality PDF data

Pair distribution function (PDF) data provides information about local, medium, and average long-range atomic structures simultaneously, unlike powder diffraction which can only be applied to materials that have long-range order. As a result, the PDF technique can be applied to disordered materials, including glasses and liquids, as well as ordered materials such as crystals. Catalytic processes, nuclear waste storage, digital storage media, multiferroic transitions, heavy metal sequestration in clays, and the absorption of medications in the human body are among the many processes that depend on the local atomic environments that PDF methods reveal.

The resolution of a PDF, Δr, is dominated by the maximum scattering vector magnitude, Q_{max}, over which the scattering data is collected; this can be approximated to $\Delta r \approx 2\pi/Q_{max}$. In a scattering experiment, $Q_{max} = 4\pi \sin \theta_{max}/\lambda$, where θ_{max} is the maximum scattering angle collected and λ is the wavelength of the radiation. For quality PDF data with sufficient resolution for a wide range of samples, a Q_{max} in excess of 25 Å^{-1} is highly desirable. Data collection at a synchrotron using a large area detector (approximately 400 mm × 400 mm) allows for relatively rapid PDF data acquisitions [1], but typically limits θ_{max} to around 45° to

#362589 https://doi.org/10.1364/OE.27.016121
Journal © 2019 Received 15 Mar 2019; revised 9 May 2019; accepted 9 May 2019; published 22 May 2019

60°. The PDF technique therefore works best if X-rays of energy over 40 keV are used. X-ray scattering intensity at high Q is very weak, the accurate measurement of which is compounded by the relatively weak interaction of high energy X-rays with most materials. The optics for a PDF beamline must therefore have efficient optics to effectively concentrate a high flux onto the sample to ensure an acceptable signal-to-noise ratio and a good count rate.

A narrow bandwidth is not necessary for many PDF studies. Bandwidth contributes to the resolution of the scattering data, and a lower resolution results in a damping of the PDF data as a function of r. For example, with 0.2% bandwidth, one can measure atomic correlations up to 100 Å before the PDF signal is supressed, whereas a 2% bandwidth allows measurement of atomic correlations up to 10 Å. Depending on the system being studied, it may only be the low-r region of the PDF data which is of most interest. The benefit of an optical design that permits such high bandwidths is that it would allow measurements with a very high flux and therefore short data collection times.

1.2 Beamline design

The X-ray pair distribution function (XPDF) beamline I15-1 at the Diamond Light Source (DLS) synchrotron was commissioned in late 2015 and has been accepting users since. It is a side station of the Extreme Conditions beamline I15 and takes X-ray beam from I15's multipole superconducting wiggler, which has 24 periods of 60 mm length and a peak field of 3.5 T (see Fig. 1 for a schematic of the beamline).

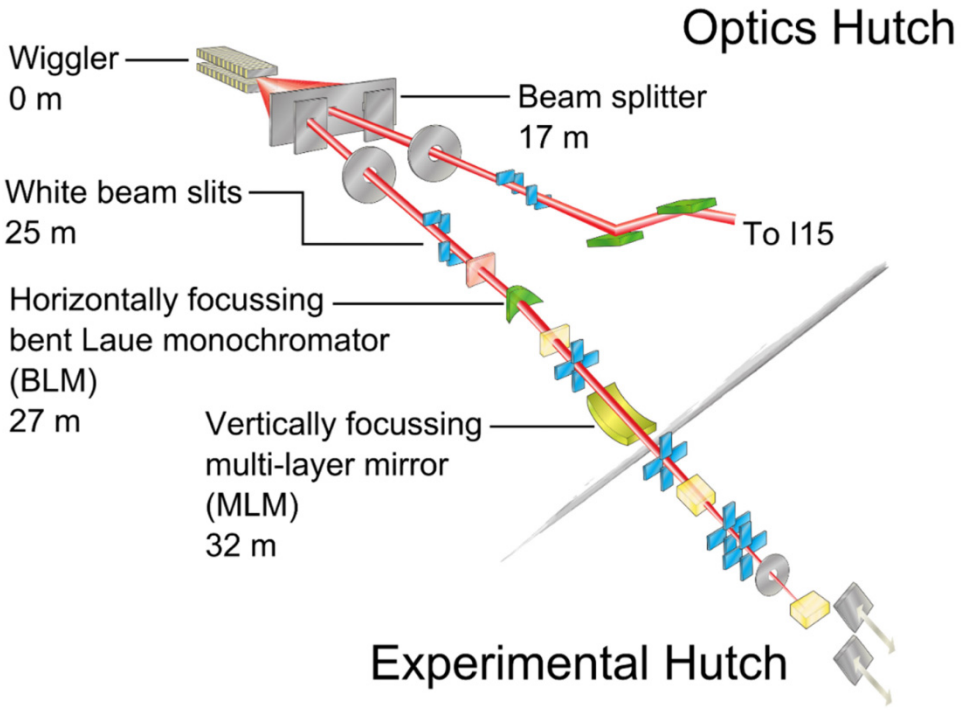

Fig. 1. Schematic of the I15-1 side station. The main station I15 lies directly along the wiggler's central axis. The I15-1 side station lies 1.5 mrad horizontally off the central axis. The divergent X-ray beam (0.5 mrad H × 0.2 mrad V) that enters I15-1 through the beam splitter is first collimated with white beam slits (typically 0.04 mrad H × 0.13 mrad V), horizontally focused by the bent Laue monochromator [2] and then vertically focused by the multilayer-coated mirror described in this paper.

Optics EXPRESS

A wiggler was chosen as I15-1's source because, unlike standard synchrotron bending magnets or undulators, it can produce a large flux of X-rays of high photon energy even at DLS's 3 GeV storage ring, allowing collection of scattering data up to a large Q_{max} and thus improving the resolution of the measured PDF. The requirement for high flux means that the wiggler's output X-ray flux, which is distributed over a large area, must be as efficiently collected and focused as possible. The I15-1 beamline optical layout was designed to focus a 0.5 mrad (H) × 0.13 mrad (V) section of the divergent wiggler beam into a spot of 680 μm (H) × 20 μm (V) full width at half maximum (FWHM) size. The minimum horizontal focal spot size is primarily determined by the oblique angle, 1.5 mrad off the central axis of the wiggler, at which the front end aperture of I15-1 views the extended wiggler source. The small target size for the beam in the vertical plane requires high demagnification factors from the condensing optics. The position of the focal spot along the beamline has to be varied controllably and continuously over a range of almost 1 m between the sample and the furthermost detector position. The adjustable focal position permits experiments to be optimised to deliver the highest reciprocal space resolution, which is achieved when the focus is on the detector, or the highest mapping resolution, which is achieved when the focus is on the sample. The optical design of I15-1 requires a bandwidth that is controllable from about 0.2% to 2% of the selected X-ray energy. The main contribution to this comes from the horizontal opening of the white beam slits.

Devising a set of optical components that would simultaneously satisfy the requirements for high flux, high energy with a wide bandwidth, and efficient and variable focusing was a significant challenge that could not be met by designs used on most other beamlines. A single-bounce, meridionally bent Laue crystal monochromator was selected to provide the necessary horizontal deflection (away from the main I15 beamline path) and focusing in the horizontal plane. It is composed of three crystals, each of which can be inserted into the beam to select X-rays with one of three energies: 40.0, 65.4, and 76.6 keV. A description may be found in [2]; since this publication, the monochromator has been successfully commissioned and will be detailed in a future publication.

Vertical focusing of high energy X-rays from such a large aperture also required a non-standard solution. Focusing delivered through X-ray mirrors that apply Fresnel total external reflection suffer from excessively shallow critical angles even when coated with metals of high electron density such as platinum. Therefore, it is impractical and technically prohibitive to make them long enough to accept the large-area wiggler beams that enter I15-1. Compound refractive lenses have insufficient ability to refract X-rays of the energies suitable for PDF measurements without using a very large number of lenses of very short radius, which raise absorption losses and limit the effective aperture even further below the already insufficient geometrical aperture of less than 1 mm provided by Pt-coated mirrors. The solution was a 1m long multilayer-coated bimorph mirror, the first of such length at a synchrotron beamline. By making the graded multilayer's period small enough, it was possible to raise the Bragg angle of the multilayer's first-order reflection to 4.2 mrad, large enough to allow a mirror of useful optical length of 1 m to accept the central 0.13 mrad vertical aperture of I15-1. (This accounts for 77% of the total wiggler flux that passes the beam splitter, which is a fixed mask with two apertures, one for each beamline.) We stress here that such an active optical size is easily achieved for bimorph mirrors, but is unprecedented for multilayer coatings on an optical component in active use at a synchrotron beamline.

Multilayer coatings have often been applied as wide bandpass monochromators (~1-2%) at DLS and elsewhere [3], which makes them ideal for the bandwidth measurements possible on I15-1. The application of multilayer coating techniques to optical components of increasing size continues to make progress. Störmer *et al* [4] have reported the fabrication of a 500 mm long, laterally graded Ru/C multilayer mirror and its successful testing with Cu $K\alpha_1$ (8.048 keV) and Mo $K\alpha_1$ (17.48 keV) X-rays. The coating of silicon substrates with boron carbide has been carried up to a 1500 mm length by Störmer *et al* [5]. To make an

elliptical mirror's focal length adjustable, bending can be applied using either mechanical actuators (on rectangular or more exotically shaped substrates) or bimorph actuators [6]. A bimorph mirror with 16 actuators was chosen because it can be set for a large range of focal lengths with almost ideally elliptical shaping of its reflecting surface, and also corrects polishing errors on the reflecting surface down to lengths of approximately 70 mm as well as its own sag under gravity almost up to its ends. In addition, compensation of wavefront distortions introduced by other optical elements is possible (although not demonstrated in this work). This combination of multilayer coatings with a bimorph construction is unique and has proved to be a successful optical element for the I15-1 beamline.

1.3 Design specification of the vertically focusing, multilayer-coated bimorph mirror

The history and design of this novel mirror, the first of its kind, was described previously in [7]; a summary is provided here. Figure 2 shows a diagram of the completed mirror. Manufacture of the multilayer-coated bimorph mirror was led by Cinel Strumenti Scientifici s.r.l. (Padua, Italy). Cinel constructed the accompanying positioning mechanics and vacuum equipment. Thales-SESO (Aix-en-Provence, France) procured, shaped and polished the single-crystal silicon substrate. The substrate is 1100 mm long × 50 mm wide × 40 mm thick. The reflecting surface was pre-shaped and polished into an ellipse that can focus the wiggler source (31.8 m upstream) to a position 4 m downstream when tilted to the specified 4.2 mrad grazing angle to the incident beam. The optically active area of the polished substrate is 1000 mm long × 30 mm wide. The optically active area was specified to have a root mean square (rms) micro-roughness no greater than 2 Å in order to guarantee the high bandpass and reflectivity of the multilayer reflections. The maximum meridional and sagittal slope errors were specified over the full elliptical bending range to be below 1.0 μrad and 10 μrad rms, respectively, in order to keep the focal spot within specifications. Rigaku Innovative Technologies (Michigan, USA) coated the substrate with three parallel, 10 mm wide, periodic multilayer stripes running along its length: the multilayer compositions were Ni/B_4C for 40.0 keV, W/B_4C for 65.4 keV, and Pt/B_4C for 76.6 keV. A value of 0.5 was selected for Γ, the ratio of the high-density layer's thickness to the multilayer period. Values of Γ measured by Rigaku using reflectivity of Cu Kα X-rays were 0.512, 0.520, and 0.520 for the Ni/B_4C, W/B_4C, and Pt/B_4C multilayers, respectively. The variation of the grazing angle of incidence of the X-ray beam along the mirror's length (3.991-4.455 mrad, i.e. a range of 0.464 mrad) is several times larger than the widths of these multilayer reflections as calculated by IMD [8]. These widths are 0.137, 0.110, and 0.091 mrad for Ni/B_4C at 40.0 keV, W/B_4C at 65.4 keV, and Pt/B_4C at 76.6 keV, respectively, if micro-roughness is neglected. Non-zero micro-roughness will further reduce these widths. Therefore, the period of all of these multilayers had to be graded along the mirror's length so that the entire mirror meets the multilayers' Bragg condition, or as close to it as possible once it is shaped to the required ellipses. Initial calculations showed that the bandpass may be increased slightly through depth grading of the multilayer; however, since this was at the cost of peak reflectivity and was seen to add considerable complexity and technical risk for little gain in most beamline applications, it was decided that all multilayers would be kept uniform with depth. Table 1 shows the specification of the three multilayer coatings. After the coating, Thales-SESO glued the piezoelectric bimorph actuators to the sides of the substrate and attached a set of Cu braids for thermal stabilization of the mirror. The pre-shaped ellipse of the substrate can further be modified using the bimorph actuators to focus to a position between the sample (3.8 m downstream) and the detector (up to 4.7 m downstream), hence over a range of 0.9 m. The bending to be applied by the bimorph to the ML coatings is thus minimized. The divergence of the reflected beam from the mirror will therefore vary from 1.105 mrad when the focus is on the sample to 0.894 mrad when the focus is on the detector. Sixteen electrodes are available to change the focusing ellipses and to correct local figure errors on its reflecting surface. The electrodes can accept voltages between −1500 V and + 1500 V. An HV-

ADAPTOS (S.RI.tech, Italy) high-voltage bipolar power supply (HVBPS) was selected for its programmable voltage slew rates and its potential to compensate hysteresis and piezo creep. Reports on continuing work to add functionalities that will make the HVBPS faster and more accurate for dynamical adaptive optics have recently been published [9,10].

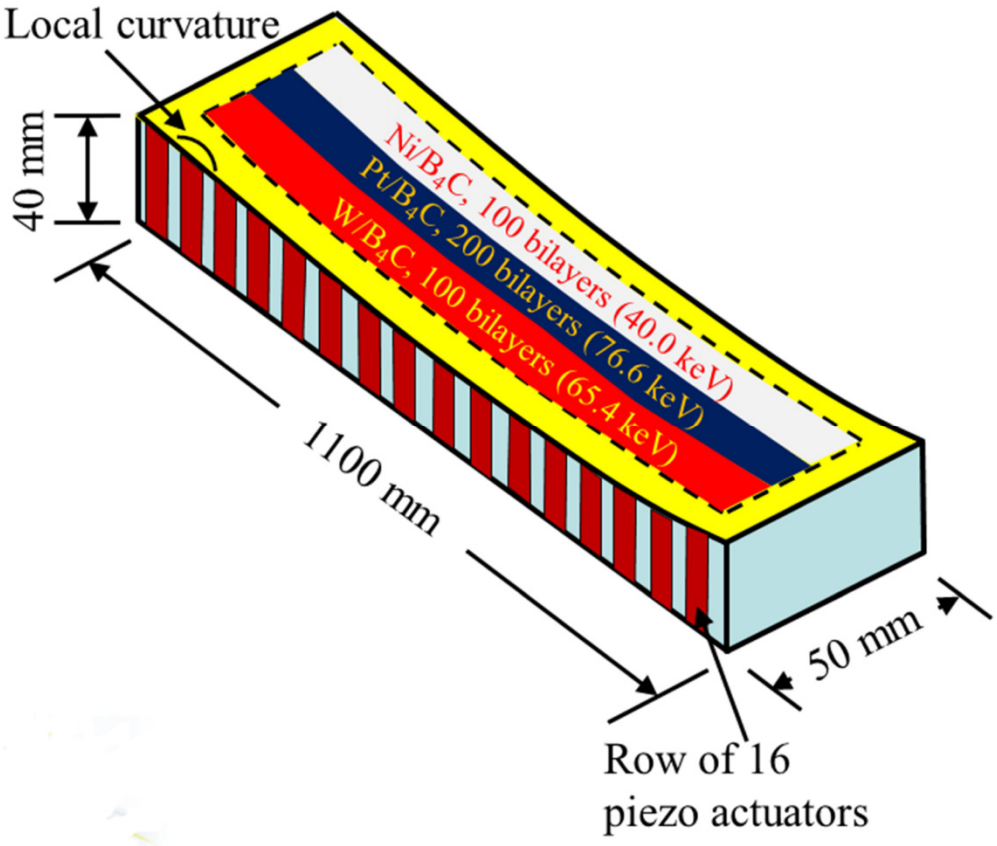

Fig. 2. Schematic of the complete multilayer-coated bimorph mirror of the Diamond Light Source beamline I15-1. An example of a local curvature introduced to the reflecting surface by one of the piezo actuators is shown.

Table 1. Specifications of the three multilayer coatings on the I15-1 vertically focusing bimorph mirror as determined by Rigaku Innovative Technologies. The grazing angle of incidence at the center of the mirror's active area is 4.2 mrad. The gradient of each multilayer's period was calculated for a focal distance of 4 m from the mirror's center. *Γ* is the ratio of the high-density layer's thickness to the multilayer period.

Multilayer	Energy (keV)	Number of bilayers	Measured *Γ*	Period (Å)		
				Upstream edge	Center	Downstream edge
Ni/B_4C	40.0	100	0.512	38.8	36.9	34.7
W/B_4C	65.4	100	0.520	23.7	22.6	21.3
Pt/B_4C	76.6	200	0.520	20.3	19.2	18.1

1.4 Ex situ metrology during manufacturing and prior to beamline installation

Thales-SESO verified that the micro roughness of the bare substrate, as measured on a regular grid of 15 equally spaced points within the active area, ranged from 1.05 Å to 1.75 Å rms; this was within the specified value of 2 Å rms required to allow the multilayer coating to meet reflectivity specifications. Thales-SESO measured the sagittal slope error across the active

area's center and at its two longitudinal ends. Their results ranged from 4.0 µrad to 4.9 µrad rms, which was well within the <10 µrad rms specified. Both the micro-roughness and the sagittal slope error therefore complied with the design specifications. Rigaku Innovative Technologies applied the required multilayer coatings and performed X-ray reflectivity measurements, using the Cu Kα emission line of an X-ray tube, to determine the accuracy of the laterally graded period of the multilayer coatings. According to their measurements, deviations from the specified period across the length of the mirror ranged from –0.28% to +0.31% for the Ni/B_4C multilayer, from –0.47% to + 0.06% for the W/B_4C multilayer, and from –0.42% to + 0.14% for the Pt/B_4C multilayer.

Final site acceptance tests of the coated mirror's figure after Thales-SESO glued the bimorph actuators to its sides were carried out on the Diamond Nanometre Optical Metrology (NOM) slope measuring profiler [11] in the Optical Metrology Lab at DLS with the mirror facing upwards, in its I15-1 operating geometry. With all the bimorph's voltages left unpowered, the parameters of the best-fit natural ellipse of the mirror were (p = 31.773 m, q = 3.810 m, θ = 4.2 mrad,), already very close to what was required by the beamline layout in Fig. 1. Here p is the distance from the X-ray source to the center of the mirror, q is the distance from the center of the mirror to the focus, and θ is the grazing angle of incidence of the X-ray beam at the center of the mirror. At q = 3.827 m, the tangential slope error over the active area was reduced to 0.68 µrad rms by adjustment of the bimorph voltages applied to the electrodes using the well-known interaction matrix method [12]. Because this was already well below the specified tolerance, and to minimise the contact between the multilayer coating and air, the NOM-based measurements and optimizations were not pushed further. Post-measurements simulations indicated that additional iterations of the interaction matrix method to refine the voltages could have reduced the slope error to even better than 0.5 µrad rms at the ellipse of weakest curvature (q = 4.827 m). Hence, based on past experience, we expect that a similarly low residual slope error would be achieved over the full range of ellipses within the dynamical range of the bimorph actuators.

After these optical measurements, the mirror was installed on the I15-1 beamline. Figure 3 is a photograph of the completed mirror mounted in its holder and UHV positioner at the beamline.

Vol. 27, No. 11 | 27 May 2019 | OPTICS EXPRESS 16127
Optics EXPRESS

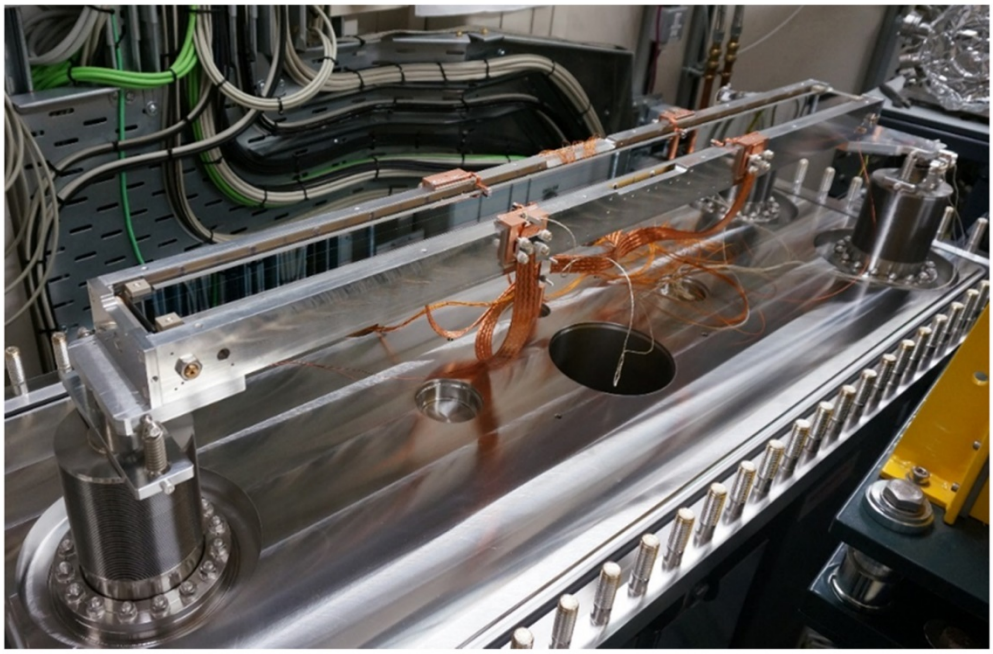

Fig. 3. Photograph of the vertically focusing, multilayer-coated bimorph mirror in its holder and UHV positioners in the DLS beamline I15-1. The three vertical jacks, one in the front of the photo and the other two in the rear, align the mirror in pitch, height, and roll. Stripe change (horizontal translation) and yaw are actuated by means of two in-air translations (upstream and downstream, not shown). The positioning jacks and stages are directly connected to the granite support and decoupled from the vacuum vessel. The Cu braids visible in the photo are used for thermal stabilization of the mirror.

2. X-ray measurement procedures

In this section we report an optimal focal performance of the multilayer-coated bimorph mirror at 76.6 keV before measurements with X-rays of the three specified energies under the standard operating conditions of the beamline. For each stripe, focal spot sizes at three distances covering the space between the sample and the furthermost detector position were measured using knife-edge scans. Scans of the reflectivity of each stripe versus incidence angle at a series of positions along the mirror's length were measured and compared with pencil beam scans that show the figure errors of each stripe. In this way, both slope errors of the substrate and spacing inaccuracies in the multilayer coatings can be deterministically measured.

During operation, the volume inside the vessel containing the multilayer mirror is maintained at 2×10^{-9} mbar by a single ion pump with a pumping speed of 500 L/sec.

2.1 Beamline setup and energy calibration

The optimal focal performance of the mirror was characterised with X-rays of 76 keV and with the monochromator crystal unbent to reduce any impact on the incoming wavefront.

By contrast, the mirror's performance under authentic operating conditions was characterized with the beamline in a "typical" user setup as much as was practicable. The white beam slits were set to deliver a divergent beam of 0.04 mrad H × 0.13 mrad V. The monochromator crystals were meridionally bent to partially focus the beam in the horizontal plane, and to increase the bandwidth [2]. Please note that this has a hitherto uncharacterised effect on the wavefront of the beam impinging the mirror.

To accurately measure the energy of the monochromatic beam, a multi-distanced 2D powder diffraction calibration method was employed [13] as implemented in the DAWN software [14]. This entails collecting a number of 2D powder diffraction patterns at known detector distance intervals, and refining an energy and detector orientation to best explain the observed peak positions. The absolute accuracy of the energy calibration method is estimated to be within 10 eV.

2.2 Optimal focal profile measurements

Knife-edge scans of the vertical focal profile were taken using a tungsten carbide knife edge (10 mm thick, 0.5° profile). The mirror profile was optimised using piezo response functions collected with X-ray data to focus on the sample position (3.8 m downstream from the mirror) and the slit was placed at this position. Scans were performed with the slit entering the beam from below.

2.3 Operating focal profile measurements

Knife-edge scans of the vertical focal profiles were taken using a gold cylinder of 5.08 mm diameter driven by a piezo stage in steps of 2 μm. Vertical slits just upstream from the mirror were opened to 4.0 mm in order to ensure full illumination of the optically active length of each stripe. The focal profiles were measured at three positions:

Near: at the sample position (3.8 m downstream from the mirror)

Mid: 460 mm downstream from the sample position (4.26 m downstream from the mirror)

Far: 920 mm downstream from the sample position. (4.72 m downstream from the mirror)

Before taking the first set of knife-edge scans at 76.6 keV on the Pt/B_4C stripe, the voltages applied to the bimorph actuators were roughly optimized by consecutive knife edge scans at slightly different voltage sets. The voltage set that produced the narrowest spot at the knife edge was chosen for data collection. However, when translating the mirror first to the W/B_4C stripe for tests at 65.4 keV and finally to the Ni/B_4C stripe for tests at 40.0 keV, the voltages were *not* adjusted again except for a slight change of the overall curvature for the mid scans at 40.0 keV. Instead, the same voltage sets were used on all three stripes in the near, mid, and far focus scans, without compensating for the slight mirror surface inhomogeneity in the sagittal direction due to residual polishing errors. The focal spot could have been optimised further to compensate for the effect of bending the monochromator crystal, so that the measured vertical profiles of the beam reported here may be wider than the best possible value. However, rapid switching from one energy to another, rather than the achievement of ultimate performance for each individual energy and focal length, was our purpose. As indicated by the offline NOM-based measurements, fine tuning of the mirror's figure error at each stripe using pencil beam scans, and thorough optimisation to the incoming wavefront from the bent monochromator crystal, could therefore further improve the focal profiles shown here.

X-rays of the high energies selected here are challenging to measure with knife-edge scans because they can pass easily through the thin section close to the rod's edge. Therefore, data that have been deconvoluted from the effect of transmission will be presented. Plots of transmission of a ray versus the ray's displacement from the gold rod's edge are shown in Fig. 4 for all three selected energies.

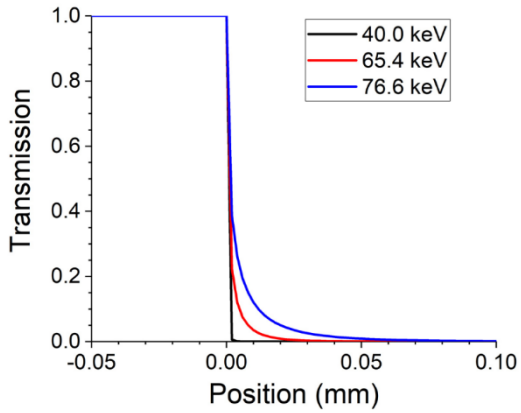

Fig. 4. Theoretical transmission of X-rays of the three operational energies as a function of distance from the edge of an ideal gold cylinder of 5.08 mm diameter. The width of the X-ray beam is neglected. Positive values of position are oriented into the cylinder. Attenuation lengths of 39.9 µm for 40.0 keV, 134.8 µm for 65.4 keV, and 212.8 µm for 76.6 keV were obtained from the software package XOP [15].

To distinguish between tails in the beam profile caused by imperfect blocking of the beam at the edge of the cylinder and tails that are genuinely part of the focused beam profile, two knife-edge scans were collected on each stripe at each position downstream from the mirror. In the first scan, the gold cylinder enters the beam from below ("falling edge") and in the second scan, the gold cylinder exits the beam from below ("rising edge"). The knife-edge scans at 76.6 keV and 65.4 keV were deconvoluted using the transmission functions plotted in Fig. 4. Those at 40.0 keV required no deconvolution because the transmission is to a very good approximation a step function that drops off very sharply at the edge of the gold cylinder.

2.4 Reflectivity scans: measurements versus position along each stripe's length

The primary slits of the I15-1 beamline, located 7 m upstream from the mirror as shown in Fig. 1, were opened to 0.5 mm (H) × 3.5 mm (V) in order to fully illuminate the active length of the mirror. To normalize the reflectivity to the intensity of the incident beam, the mirror was withdrawn from the beam and the scanning slit, which was closed to a 30 µm vertical width and placed 1174 mm upstream from the mirror's center, was scanned vertically in 60 µm steps over a 4.5 mm wide range across the beam's central maximum. This corresponds to a lateral resolution of 7.4 mm along the mirror length, with illuminated areas of 0.64 mm width. The transmitted intensity as a function of scanning slit position was measured with a diode. Slit motor encoder positions were used to normalise any deviation in intensity arising from each slits blade moving independently, rather than being directly coupled in a piggyback design.

The voltages applied to the bimorph were set so that the mirror would focus the beam 250 mm downstream from the sample position, about halfway between the near and mid positions in the knife-edge scans. It is here that the multilayer gradient design is optimized, ensuring that the reflectivity peaks at nearly the same pitch angle along the mirror's entire active length, when not affected by the substrate's figure error, micro-roughness, or by imperfections in the deposited multilayer's spacing.

A series of reflectivity scans was then performed on all stripes at their corresponding energies in Table 1. The mirror was centered vertically on the beam, and the scanning slit was opened to the same width and scanned through the same set of positions as in the normalization scan. At each position of the slit, the pitch angle of the mirror was scanned from 4.45 mrad to 4.00 mrad in steps of 0.004 mrad at 40.0 keV and 65.4 keV, and from 4.35

mrad to 4.10 mrad in steps of 0.003 mrad at 76.6 keV. The reduced range and smaller step of the 76.6 keV reflectivity measurements take into account the relatively small angular width of the multilayer reflection at such a high photon energy.

The center of rotation of the mirror's pitch rotation coincides with the center of the mirror's active surface. Therefore, in all reflectivity scans except the one at the very center of the mirror, the illuminated region of the mirror changes as the mirror's pitch angle is scanned. This is taken into account by dividing the slit position by the sine of the pitch angle at every point in each reflectivity scan. In the reflectivity scan performed when the scanning slit is placed at a specified position, the diode reading of the reflected beam is divided by the equivalent reading from the normalization scan. The resulting normalized reflectivity is finally plotted against both the calculated position along the mirror's surface and the pitch angle.

2.5 Pencil beam scans

Narrowing the scanning slits to a vertical width of 30 μm, X-ray pencil beam scans of each stripe were taken to measure its figure errors. An X-ray imaging system consisting of scintillator, lens, and camera collected the images of the reflected beam at each position of the scanning slit, which was moved in steps of 20 μm to cover the full active length of each stripe. The conversion of pixel size to distance in the field of view, accounting for the lens magnification, was measured as 5.2 μm/pixel. In this way, the reflected beam position determined from each image in the pencil beam scan was converted to displacement. Using a measured distance of 4.077 m from the mirror to the scintillator, the local slope error on the mirror was then calculated from the beam displacement on the scintillator. On each stripe, two pencil beam scans were measured. In the first scan, all voltages on the bimorph were set to 0 V. In the second scan, the voltages on the bimorph were interpolated from reference values determined by interaction matrix calculations at several focal distances. The mirror then focused the beam at approximately 250 mm downstream from the sample as in the reflectivity scans, although a full optimisation was not performed for lack of time as it was not necessary for the conclusions of this report. After each change of voltages, the mirror was allowed to settle for 5 minutes before the start of the pencil beam scan.

3. Results and discussion

3.1 Focal profiles

The optimal vertical focal profile collected using the procedure outlined in §2.2 is shown in Fig. 5(a). The vertical FWHM size of the wiggler photon source is calculated by SHADOW as 15.6 μm when the electron beam emittance and size are taken into account. The geometrically demagnified FWHM source size will then be approximately 1.9 μm, much smaller than the image blurring caused by even the lowest possible slope errors. The assumption of a 0.8 μrad rms tangential slope error on the mirror, a conservative estimate made early in the design planning, yields a theoretical beam size of about 2(2.3548)(0.8 μrad)(3.5 m) = 13.1 μm when the focal spot is 3.5 m downstream from the mirror. This agrees well with the value of 12.6 μm calculated from a Gaussian fit to the SHADOW simulation. On the other hand, the measured width of the best Gaussian fit to the knife-edge scan is 9.7 μm, which indicates that the rms tangential slope error was approximately 0.53 μrad. This is consistent with the pencil beam scan data shown below. The knife-edge scan is not deconvoluted because the tungsten carbide knife edge blocks 76.6 keV X-rays as effectively as the gold rod blocks 40 keV X-rays.

For completeness, even though the X-rays are focused by the bent Laue monochromator and not by the multilayer mirror, Fig. 5(b) displays the horizontal profile of the focused beam of 76.6 keV X-rays at the Near position. It is measured by an X-ray imaging system of spatial resolution 5.2 μm/pixel, since the full width at half maximum of 585 μm is too large to be

measured using a knife-edge scan. The profile appears smooth, and its width is well below the 680 μm value that was specified for the beamline's design.

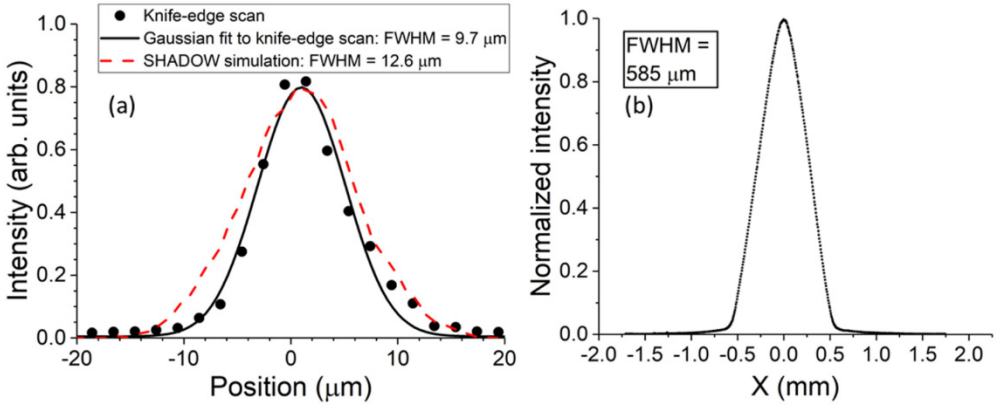

Fig. 5. (a) Vertical knife-edge scan (circles) compared with its Gaussian fit (solid curve, FWHM = 9.7 μm) and a SHADOW ray-tracing simulation (dashed curve, FWHM = 12.6 μm) for the Pt/B4C stripe at the focus 3.82 m downstream from the multilayer mirror. In the SHADOW simulation, the vertically focusing mirror is assumed to have a rms tangential slope error of 0.8 mrad and to be focusing the beam 3.5 m downstream. The SHADOW simulation has been smoothed so that statistical noise is removed without altering the overall width of the theoretical beam profile. (b) Horizontal focused profile of 76.6 keV X-rays measured by an X-ray imaging camera with a spatial resolution of 5.2 μm/pixel at the Near position.

All the operational knife-edge scans (see §2.3) collected on the mirror were compared before and after deconvolution. They have been omitted here for brevity but are available on request. The raw profiles before deconvolution show a strong tail at 76.6 keV, a somewhat weaker tail at 65.4 keV, and only a very weak tail at 40.0 keV. This is exactly what one would expect from the transmission calculations in Fig. 4. Also as expected, the tail appears on the side of the peak on which the beam is passing through the gold cylinder very close to the edge: the positive side in the falling-edge scans, and the negative side in the rising-edge scans. This confirms that transmission through the gold cylinder close to its edge does indeed affect the results and must be taken into account and corrected.

The deconvolution of the knife-edge scans at 76.6 keV and 65.4 keV removes the tail caused by partial transmission through the rod, as demonstrated in Fig. 6. Small structures remaining around the peak may be caused by deviations of the gold cylinder from the ideal round shape rather than scatter from the mirror's surface.

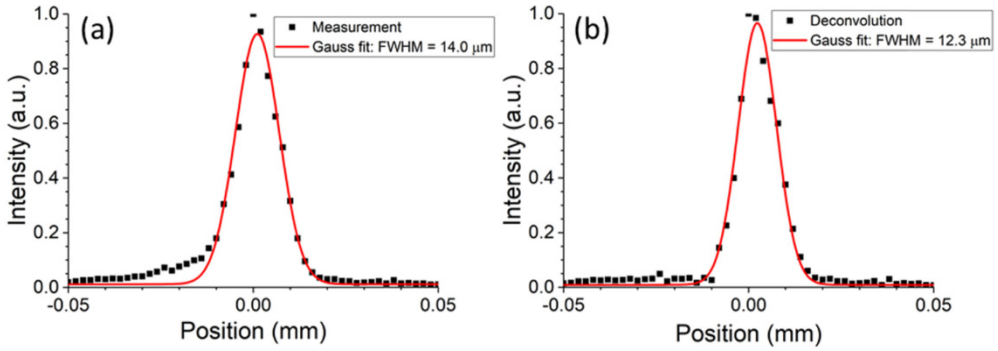

Fig. 6. Example of deconvolution of knife-edge scan using gold rod: (a) raw data and (b) deconvoluted result of the rising-edge scan of the 76.6 keV X-ray focus at the Mid focal position.

The deconvoluted rising-edge scans at 76.6 keV and 65.4 keV, and the raw rising-edge scans at 40.0 keV for which no deconvolution is necessary, are shown in Fig. 7. In these scans, the FWHM of the Gaussian fits to the measured beam profiles range from 10.6 µm to 14.9 µm with no clear trend depending on X-ray energy or distance from the mirror. This is not as narrow as the 9.7 µm FWHM seen in Fig. 5(a). However, all of these values are well below 20 µm, the FWHM that the mirror was originally intended to achieve. As previously mentioned, a more careful adjustment of the bimorph voltages for each specific focusing configuration and monochromator crystal bending setup might reduce the widths still more.

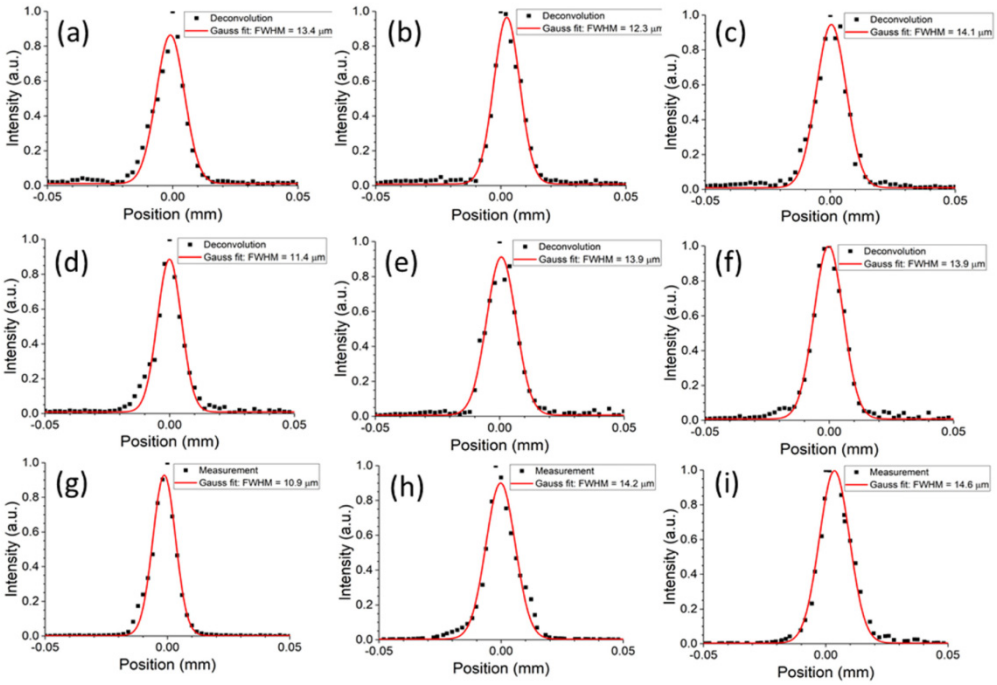

Fig. 7. Rising-edge knife-edge scans of focused X-rays using a gold rod. (a)-(c): Deconvoluted scans for 76.6 keV X-rays focused at Far, Mid, and Near focal positions, respectively. (d)-(f) Deconvoluted scans for 65.4 keV X-rays focused at Far, Mid, and Near focal positions, respectively. (g)-(i) Scans for 40.0 keV X-rays focused at Far, Mid, and Near focal positions, respectively. For these no deconvolution was required (see text).

3.2 Reflectivity and slope error

Although the reflectivity scans and the pencil beam scans were collected separately, their results are considered together because in combination they yield a more complete understanding of the multilayer mirror's overall quality. Some introductory results shown in Fig. 8 will help explain the results of this section.

Figures 8(a) and 8(b) display the tangential slope errors determined at I15-1 by the X-ray pencil beam scans on all stripes, both before and after mathematical subtraction of the best fit cylinder. There is no significant variation of the tangential slope errors across the mirror's width. Furthermore, the 0.52 µrad rms slope error obtained after subtraction of the best fit cylinder is consistent with the small focal spot in Fig. 5(a). A rough theoretical estimate of the rms width of the focal spot can be obtained by doubling the product of the optimized slope error of 0.52 µrad rms and the focal distance of 3.82 m. The FWHM can then be obtained by multiplying the rms width by $2\sqrt{2\ln 2}$, the conversion factor from sigma to FWHM for a Gaussian. Hence the estimated theoretical spot size is 2(0.52 µrad)(2.3548)(3.82 m) = 9.4 µm, just slightly below the measured 9.7 µm FWHM. The slope errors measured by the X-ray

Optics EXPRESS

pencil beam scans are to be compared with those measured *ex situ* on the Diamond-NOM in Fig. 8(c). Once the best fit cylinder (focus term) is subtracted, accounting for small errors in the experimental determination of the beam minimum waist, the slope errors measured *ex situ* and *in situ* are of similar magnitude, though of somewhat different spatial variation. Thus, the simplest explanation for the discrepancy between the slope errors measured by the X-ray pencil beam scans at slightly over 1 µrad rms, and the slope errors measured on the Diamond-NOM at 0.68 µrad rms, is that in the X-ray measurements the focus was very close to but not exactly on the imaging system's scintillator. The focal spot sizes determined from the knife-edge scans, which are somewhat larger than the minimum measured value in Fig. 5(a), are consistent with slope errors of 0.6-0.8 µrad rms, slightly lower than those measured by the X-ray pencil beam scans. This is reasonable because some care was taken to locate the focus on the knife edge as closely as time permitted. Finally, Fig. 8(d) compares the voltage sets applied to the bimorph during the measurements on the Diamond-NOM and all measurements taken with X-rays. These too are similar except at Electrode 1 where the X-ray beam is weak, indicating that the response of the bimorph both *ex situ* and *in situ* remains highly consistent. Because the voltages follow a smooth trend from one electrode to the next, and because the slope error's spatial variation occurs on scales longer than the width of an electrode, further iterations of the interaction matrix method are expected to improve on the slope errors achieved so far in Figs. 8(b) and 8(c).

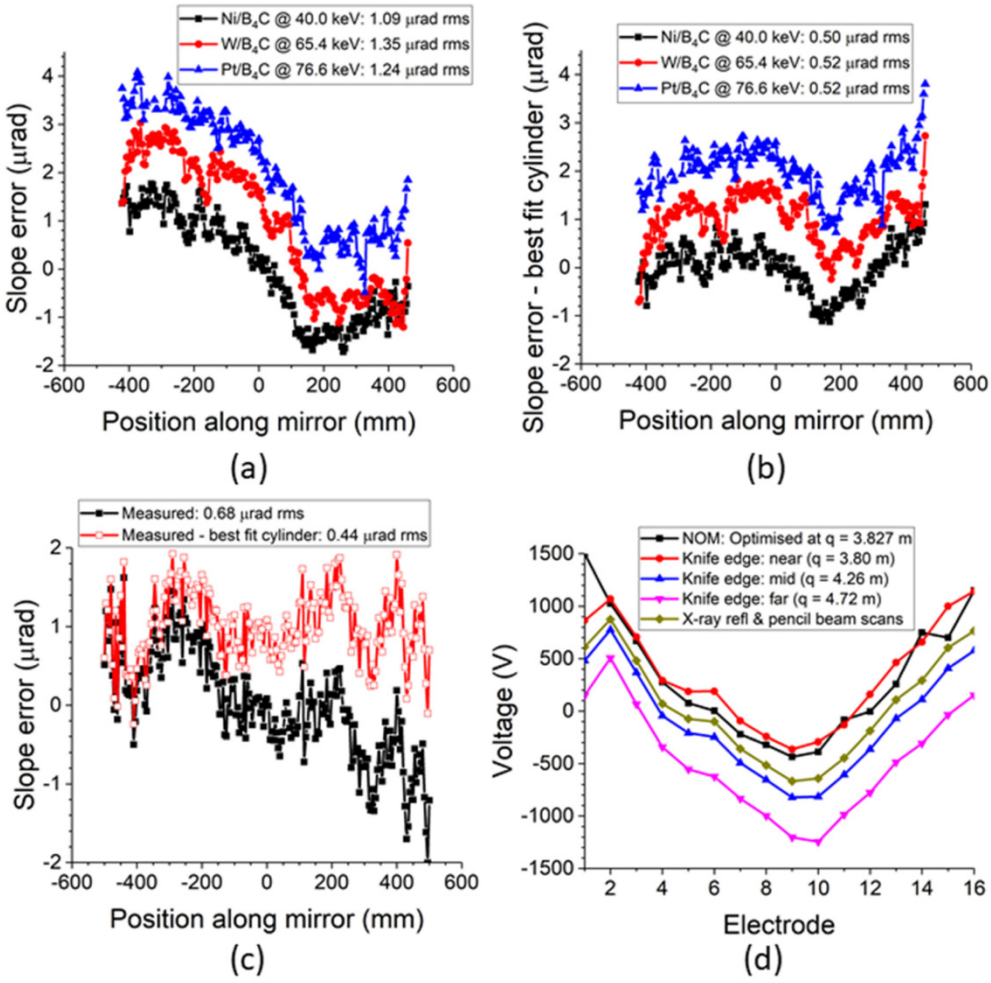

Fig. 8. (a) Slope errors determined from X-ray pencil beam scans on all three stripes. Successive plots are displaced vertically in steps of 1 μrad for clarity. (b) Same slope errors as in (a) after mathematically subtracting the best fit cylinder. (c) Slope errors measured *ex situ* on the Diamond-NOM assuming a focal distance of 3.827 m before and after mathematical subtraction of best fit cylinder. The residual is displaced upward by 1 μrad for clarity. (d) Voltage sets applied to the piezoelectric bimorph actuators on the Diamond-NOM, for all focal distances at which X-ray knife-edge scans were taken, and for the X-ray pencil beam and reflectivity scans.

Plots of the rocking curves of the multilayer reflectivity over the full length of each multilayer stripe are displayed in Fig. 9. Important statistics of these rocking curves are provided in Table 2. The average angular peak positions are all slightly above the specified operational angle of 4.2 mrad, but by no more than 0.7%. This discrepancy is unlikely to have been caused by a miscalibration of the X-ray energy, which is accurate to within 10 eV. The plots show that the angular width of the rocking curve is uniform along the mirror's length, while the maximum reflectivity of the rocking curve has at most a moderately decreasing gradient from the upstream edge to the downstream edge. Reliable comparisons of measured rocking curves with theoretical calculations are difficult because the peak reflectivity and width are highly sensitive to both substrate and interlayer micro-roughness, which could not be measured over the full active area of the mirror. Nonetheless, at the center of the mirror, where the incident beam remains at the same place on the mirror's surface throughout the

Vol. 27, No. 11 | 27 May 2019 | OPTICS EXPRESS 16135
Optics EXPRESS

scan, the rocking curves are shown in Fig. 10. Their measured widths are compared with the significantly greater theoretical widths neglecting micro-roughness in Table 2. Micro-roughness is clearly a limiting factor in the multilayer performance, especially at the very challenging 20 Å spacing of the Pt/B_4C stripe. The maximum reflectivity in the central rocking curves of Fig. 10 is given in Table 2. The measured maximum reflectivity of each rocking curve taken on all three multilayer stripes as a function of position along the mirror is plotted in Fig. 11. On all stripes, the maximum reflectivity exceeds 70% along the whole mirror.

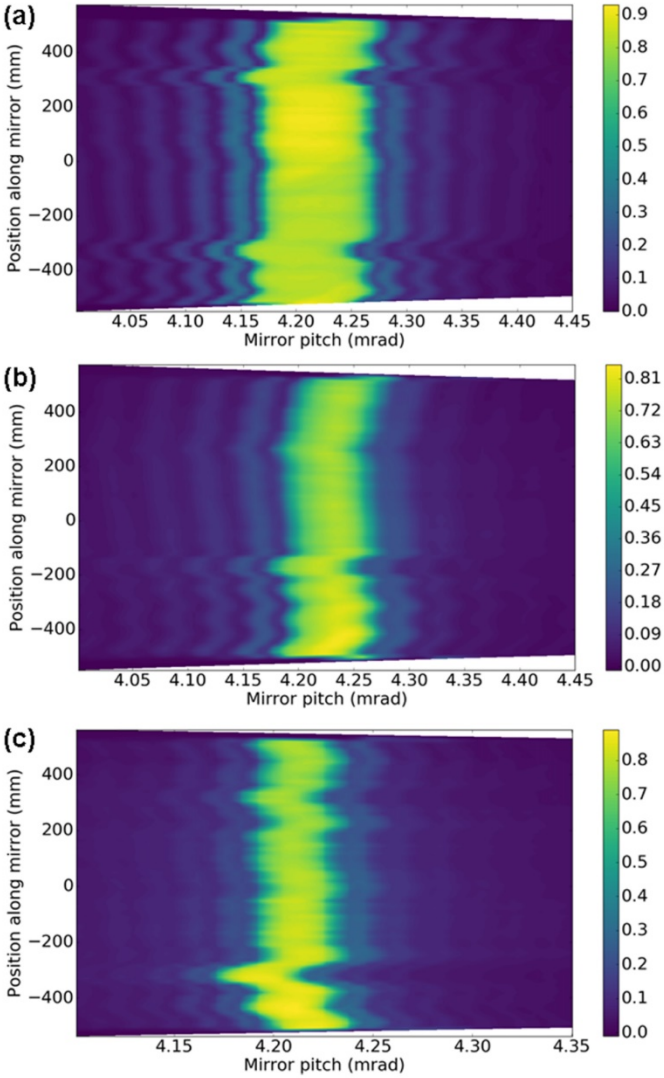

Fig. 9. Contour plots of multilayer reflectivity as a function of position along the mirror and mirror pitch angle with respect to the incident beam: (a) Ni/B_4C at 40.0 keV (b) W/B_4C at 65.4 keV (c) Pt/B_4C at 76.6 keV. The top and bottom edges of each contour plot are slanted because the beam footprint on the mirror changes its position along the mirror's length as the mirror's pitch angle is scanned.

Table 2. Statistics of measured rocking curves shown in Fig. 9.

Multilayer	Average peak position (mrad)	Width at mirror center (μrad)		Highest reflectivity at mirror center (%)	Variation of peak angle along mirror length (μrad)	
		Measured	Theoretical (zero micro-roughness)		rms	Peak to valley
Ni/B_4C	4.216	94.6	137	87.2	7.0	31.5
W/B_4C	4.230	71.4	110	74.5	6.0	30.6
Pt/B_4C	4.211	39.2	91	78.9	5.3	27.4

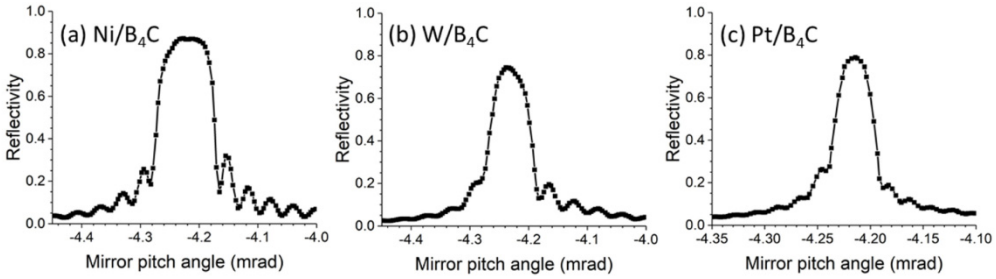

Fig. 10. Rocking curves of multilayer reflectivity at center of mirror for each stripe: (a) Ni/B_4C at 40.0 keV (b) W/B_4C at 65.4 keV and (c) Pt/B_4C at 76.6 keV.

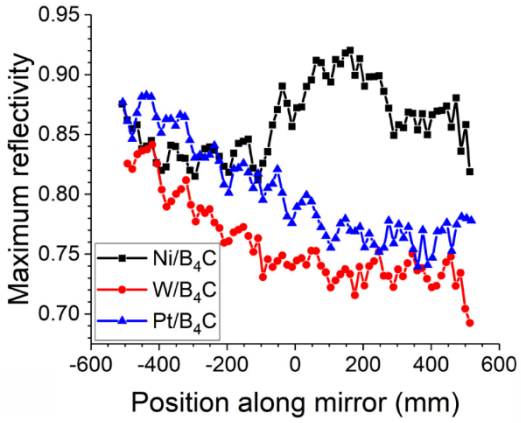

Fig. 11. Maximum reflectivity of the rocking curve taken from each multilayer stripe versus the position along the mirror.

There is, however, a local variation in the pitch angle of the rocking curve peak along the mirror's length. Errors in both slope and multilayer spacing can cause this. To separate these two contributions, a plot of the rocking curve's peak angle as a function of position along the mirror is compared with a plot of the slope error determined from the pencil beam scans on each stripe (Fig. 12). The active regions on each stripe are marked out and the rms slope errors within them were 1.06 μrad (Ni/B_4C), 1.35 μrad (W/B_4C), and 1.25 μrad (Pt/B_4C). It is emphasized that the aim of these measurements was not to obtain the lowest possible slope error, but to show that the rocking curve's peak angle varies much more strongly and rapidly along the mirror's length than does the slope error. On the Pt/B_4C stripe at 76.6 keV, where the rocking curve is narrowest, poor reflected intensity prevented the measurement of slope error data from the pencil beam scan where the rocking curve's peak angle deviates most from its average value. Fortunately, everywhere else, the variation of the rocking curve's peak angle along the mirror's length remains less than the rocking curve's width, so that the

multilayer's reflectivity remains high along the whole stripe. The variation of the rocking curve's peak angle along the length of the mirror is given in Table 2 for each stripe.

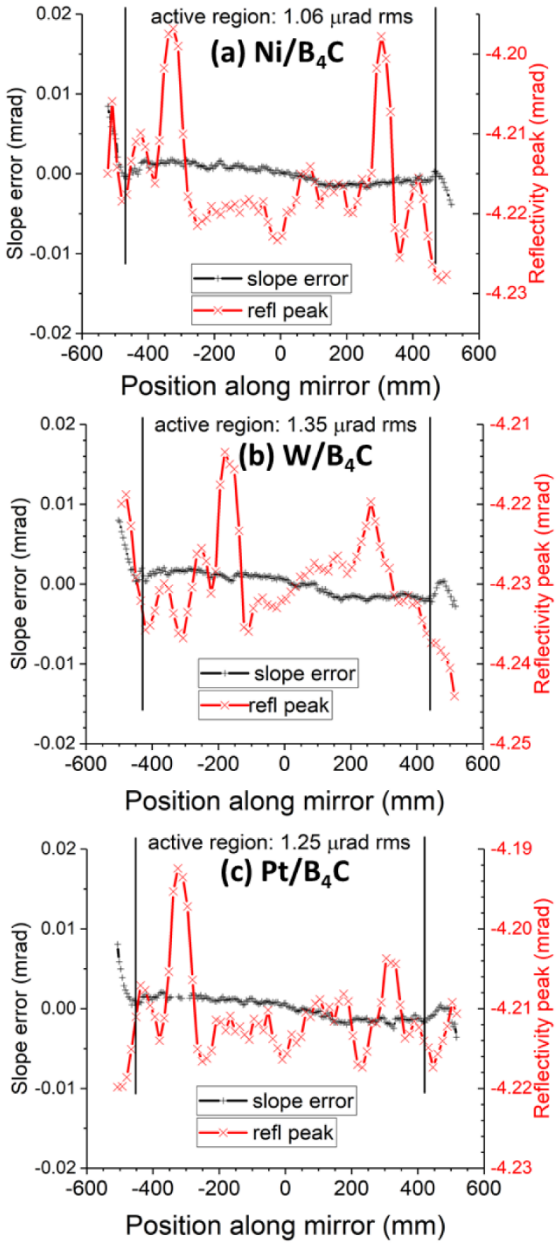

Fig. 12. Slope error measured by pencil beam scans (black + 's) compared with peak pitch angles of the reflectivity curve (red × 's) for (a) Ni/B_4C at 40.0 keV (b) W/B_4C at 65.4 keV, and (c) Pt/B_4C at 76.6 keV. Both the slope errors and the reflectivity peak angles in each graph are plotted on intervals of equal width for easy comparison. The gaps on the left-hand side of the graph in (c) are at points where the reflected intensity was too low to allow accurate determination of the beam position on the X-ray imaging scintillator. Not coincidentally, they are located where the peak pitch angle of the reflectivity deviates most strongly from its average value. The rms slope error within the active region is indicated in each graph.

The combination of both sets of data from each stripe permit the variation of the multilayer *d*-spacing to be calculated. Since this is a first-order reflection and the medium of the incident beam is vacuum, the Bragg angle θ_B for a plane wave of wavelength λ is given by

$$\lambda = 2d\sqrt{n^2 - \cos^2\theta_B}, \tag{1}$$

where n is the mean index of refraction of the multilayer. n is assumed to be uniform over each stripe. For X-rays, $n = 1 - \delta$ where $\delta \sim 10^{-6}$ or less. Differentiating the equation above and expanding to the first-order term in δ yields

$$\frac{\Delta d}{d} \approx -\left(1 + \frac{2\delta}{\sin^2\theta_B}\right)\cot\theta_B \Delta\theta_B. \tag{2}$$

The precise value of δ is uncertain because it depends on the density of the layers, which is generally lower than their materials' bulk density by an unknown amount. However, the bulk δ for the metallic materials is 1.108×10^{-6} for Ni at 40.0 keV, 7.29×10^{-7} for W at 65.4 keV, and 5.80×10^{-7} for Pt at 76.6 keV, as calculated by the utility xF1F2 in XOP [15]. For B_4C at a bulk density of 2.55 g/cm^3, δ is similarly calculated as 3.113×10^{-7} at 40.0 keV, 1.164×10^{-7} at 65.4 keV, and 8.488×10^{-8} at 76.6 keV. Because $\theta_B = 4.2$ mrad, the δ-dependent correction term has an upper bound of 0.080 for Ni, 0.048 for W, and 0.038 for Pt. These corrections are considerably smaller than 1 and are hence neglected here.

In Fig. 12, a positive slope error results in an increased upward deflection of the beam. Also, as the rocking curve peak angle increases from negative values toward zero, the grazing incidence angle of the beam on the mirror becomes shallower. Using these sign conventions, one finds that the variation in rocking curve peak angle, $\Delta\theta_{\text{rock}}$, is related to the slope error $\Delta\theta_{\text{slope}}$ and the relative variation $\Delta d/d$ by

$$\Delta\theta_{\text{rock}} = \Delta\theta_{\text{slope}} + \frac{\Delta d}{d}\tan\theta_B. \tag{3}$$

Figure 13 shows the resulting relative variation of the multilayer spacing of each stripe along the length of the mirror. The pencil beam scans were interpolated to generate estimated slope errors at each position where the peak reflectivity was measured. The only serious uncertainty was in the part of the pencil beam scan for the Pt/B_4C stripe where the reflected beam was so weak that its position at the scintillator could not be determined. These points were removed and the interpolation was carried out between the remaining points. The strong similarity of the slope errors measured on all three stripes indicates that this procedure is reasonable. The relative rms variation of the multilayer spacing is 0.135% to 0.164%, while the peak-to-valley relative variation is 0.650% to 0.812%. (These values should be compared with the 0.53% to 0.59% peak-to-valley relative variations measured *ex situ* as described in §1.4.) Note that the Ni/B_4C and Pt/B_4C stripes look quite similar, whereas the W/B_4C stripe is quite different.

As a final check of the mirror's slope error, pencil beam scans were collected on all three stripes when the bimorph actuator voltages were all set to 0 V. The results are displayed in Fig. 14. Aside from gaps in the data for the Pt/B_4C stripe where the reflected beam could not be detected, all three stripes show very similar slope errors. The slope errors measured *in situ* with X-rays are also very similar to those measured *ex situ* using the Diamond-NOM when all bimorph actuator voltages were set to 0 V [11]. Figure 15(a) compares the slope error of the Ni/B_4C stripe as measured by pencil beam scans using 40.0 keV X-rays while the bimorph was inactive (as in Fig. 14) and when the bimorph was optimized (as in Fig. 8(b)). In both cases, the cylinder that best fits the active area was subtracted so that the waviness of the mirror is clear. The sharply descending slope error at the far left and far right edges mark the boundaries of the mirror's active area, which are not shown in Fig. 8. These far edges are not normally illuminated but are displayed here for completeness. Figures 8 and 14 show that the

Ni/B_4C stripe fairly represents the other two stripes as well. Figure 15(b) shows the focal spot achieved with 76.6 keV X-rays by using the Pt/B_4C stripe with an inactive bimorph and with an optimized bimorph. The optimization of the bimorph reduces the width of the focal spot by a factor of about three. The bimorph's great importance for the achievement of a tight, clean focal spot is thus evident.

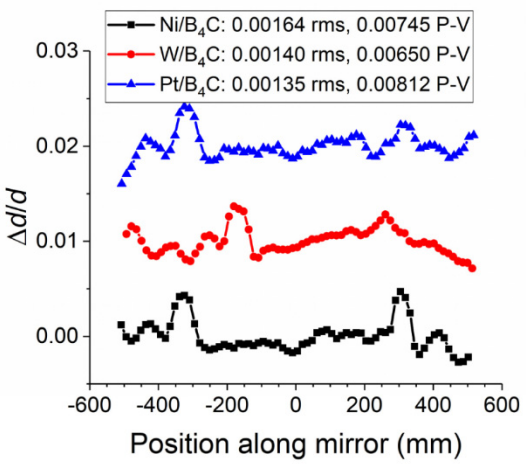

Fig. 13. Relative variation of the multilayer *d*-spacing along the length of each stripe of the multilayer bimorph mirror. Consecutive plots are vertically displaced in steps of 0.01.

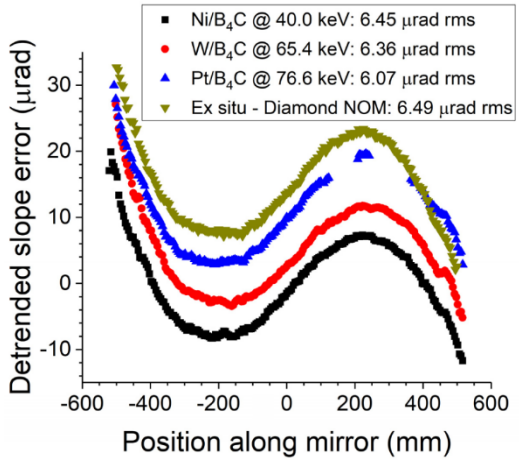

Fig. 14. Comparison of slope errors measured using X-ray pencil beam scans on each stripe with a measurement made *ex situ* on the Diamond-NOM [11] when all voltages on the bimorph actuators were set to 0 V. A best-fit linear slope, which corresponds to a uniform curvature, was subtracted from each data set to make the local slope variations clearer. On the Pt/B_4C stripe there are gaps in the data where the reflected beam was below detectable levels. Consecutive data plots are shifted upward in steps of 5 μrad.

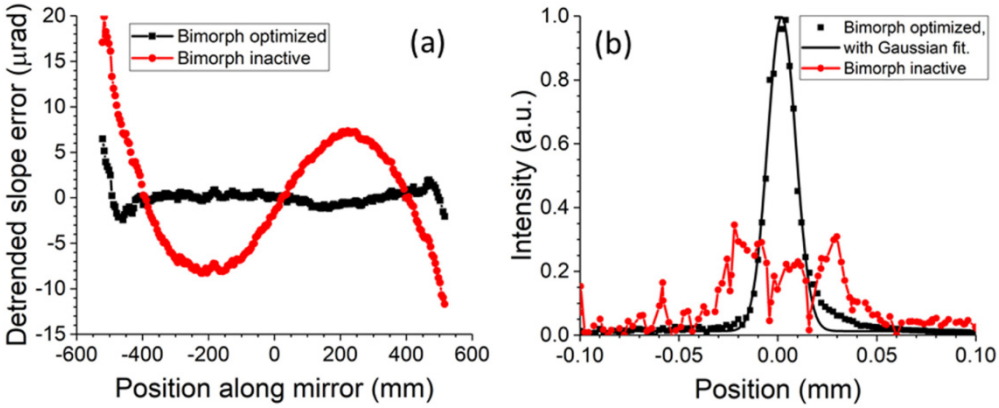

Fig. 15. (a) Comparison of the slope error of the Ni/B_4C stripe with the bimorph kept inactive and with an optimized bimorph, as measured by pencil beam scans using 40.0 keV X-rays. These results include the far edges outside the active area (not displayed in Fig. 8) for completeness, although these are not generally illuminated. (b) Vertical knife-edge scans taken of the 76.6 keV X-ray spot at the Near position after focusing by the Pt/B_4C stripe with an optimized bimorph and with an inactive bimorph. The profiles have purposely not been deconvoluted, as this is not necessary to demonstrate how effectively the bimorph improves the focus.

3.3 X-ray pair distribution function measurements

X-ray scattering and processed PDF data are shown in Fig. 16 for data collected at 76.6 keV with the mirror focused on the detector, and focused on the sample. Under standard operating conditions, using a primary slit size of 0.02 mrad horizontal × 0.13 mrad vertical, the flux of 76.6 keV X-rays in doubly focused beam on the sample position has been measured at 1.46×10^{11} photons/sec using a krypton-filled ion chamber of 200 mm path length. This high flux afforded by the large numerical aperture and high reflectivity of the multilayer-coated bimorph mean that quality scattering data can be collected with a Q_{max} in excess of 30 $Å^{-1}$, leading to excellent PDF data quality. The narrow vertical FWHM allows for scattering measurements to be performed on e.g. a single slice through the cathode layer of an *in situ* cycling lithium ion battery. The vertical focus may also find applications in other areas such as in local structure studies of coatings.

Optics EXPRESS

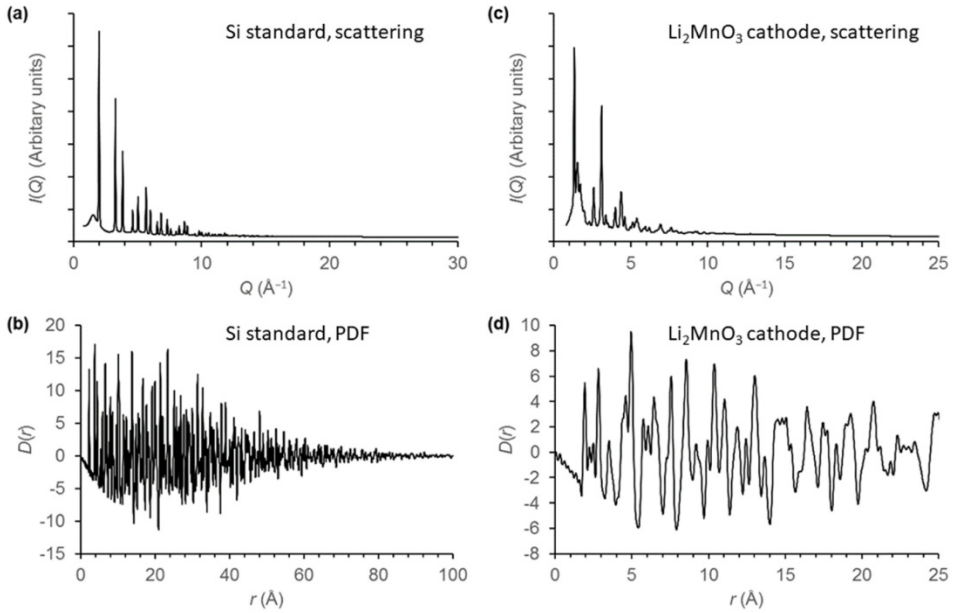

Fig. 16. Example of X-ray scattering data and corresponding PDF: (a,b) A Si standard collected in capillary geometry while focusing on the PDF detector, 200 mm downstream of the sample; (c,d) A 20 µm thick layer of a Li_2MnO_3 cathode within a battery cell collected using the mirror to focus on the cathode layer.

4. Conclusions

A unique, 1 m long bimorph mirror with three stripes of coatings, each composed of a different multilayer structure, has been manufactured and installed at the Diamond Light Source X-ray Pair Distribution Function beamline I15-1 to focus X-rays of 40.0, 65.4, and 76.6 keV. This mirror is the first of its kind to be used at a synchrotron beamline. It can accept X-rays within a vertical aperture as large as 4 mm and focus them to a spot of vertical width of ~13 µm FWHM. The focal profile's quality is well maintained without any adjustment of the bimorph voltages when the multilayer stripe in the beam is changed. X-ray pencil beam scans show that the overall slope error has been quickly brought down to almost 1 µrad rms over the full bending range and could almost certainly be further reduced to 0.5 µrad rms by careful optimization. Some additional optimisation, in particular through characterisation of the incoming wave fronts from the bent Laue monochromator crystals, could probably reduce this further still. Peak reflectivity of the multilayers at all points on the mirror exceeds 70%. Widths of the reflectivity curves fall significantly below theoretical values for an ideal multilayer, indicating that micro-roughness has a serious, though far from catastrophic, degrading influence. Although a detectable variation appears in the multilayer spacing along the mirror's length on all three stripes, it remains well below 1%, which is acceptable except for a small region on the Pt/B_4C stripe. Slope errors measured using X-ray pencil beam scans on all three stripes when the bimorph actuator voltages were all set to 0 V agreed well with each other and with data previously taken *ex situ*.

Acknowledgments

The authors wish to thank Allan Ross, Jon Thompson, Paul Roberts, and Steve Usher for their engineering and technical assistance. They also especially thank Yuriy Platonov (Rigaku Innovative Technologies) for useful and extensive discussions during the realization of the multilayer coatings.

References

1. P. J. Chupas, X. Qiu, J. C. Hanson, P. L. Lee, C. P. Grey, and S. J. L. Billinge, "Rapid-acquisition pair distribution function (RA-PDF) analysis," J. Appl. Cryst. **36**(6), 1342–1347 (2003).
2. J. P. Sutter, P. A. Chater, M. R. Hillman, D. S. Keeble, M. G. Tucker, and H. Wilhelm, "Three-energy focusing Laue monochromator for the Diamond Light Source X-Ray Pair Distribution Function Beamline I15-1," AIP Conf. Proc. **1741**, 040005 (2016).
3. A. Rack, T. Weitkamp, M. Riotte, D. Grigoriev, T. Rack, L. Helfen, T. Baumbach, R. Dietsch, T. Holz, M. Krämer, F. Siewert, M. Meduňa, P. Cloetens, and E. Ziegler, "Comparative study of multilayers used in monochromators for synchrotron-based coherent hard X-ray imaging," J. Synchrotron Radiat. **17**(4), 496–510 (2010).
4. M. Störmer, H. Gabrisch, C. Horstmann, U. Heidorn, F. Hertlein, J. Wiesmann, F. Siewert, and A. Rack, "Ultra-precision fabrication of 500 mm long and laterally graded Ru/C multilayer mirrors for X-ray light sources," Rev. Sci. Instrum. **87**(5), 051804 (2016).
5. M. Störmer, F. Siewert, C. Horstmann, J. Buchheim, and G. Gwalt, "Coatings for FEL optics: preparation and characterization of B_4C and Pt," J. Synchrotron Radiat. **25**(1), 116–122 (2018).
6. R. Signorato, O. Hignette, and J. Goulon, "Multi-segmented piezoelectric mirrors as active/adaptive optics components," J. Synchrotron Radiat. **5**(3), 797–800 (1998).
7. J. P. Sutter, P. A. Chater, R. Signorato, D. S. Keeble, M. R. Hillman, M. G. Tucker, S. G. Alcock, I. Nistea, and H. Wilhelm, "A novel, 1 m long multilayer-coated piezo deformable bimorph mirror for focusing high-energy X-rays," AIP Conf. Proc. **2054**, 030005 (2019).
8. D. L. Windt, "IMD – Software for modelling the optical properties of multilayer films," Comput. Phys. **12**(4), 360–370 (1998).
9. S. G. Alcock, I.-T. Nistea, R. Signorato, and K. Sawhney, "Dynamic adaptive X-ray optics. Part I. Time-resolved optical metrology investigation of the bending behaviour of piezoelectric bimorph deformable X-ray mirrors," J. Synchrotron Radiat. **26**(1), 36–44 (2019).
10. S. G. Alcock, I.-T. Nistea, R. Signorato, R. L. Owen, D. Axford, J. P. Sutter, A. Foster, and K. Sawhney, "Dynamic adaptive X-ray optics. Part II. High-speed piezoelectric bimorph deformable Kirkpatrick-Baez mirrors for rapid variation of the 2D size and shape of X-ray beams," J. Synchrotron Radiat. **26**(1), 45–51 (2019).
11. S. G. Alcock, K. J. S. Sawhney, S. Scott, U. Pedersen, R. Walton, F. Siewert, T. Zeschke, F. Senf, T. Noll, and H. Lammert, "The Diamond-NOM: A non-contact profiler capable of characterizing optical figure error with sub-nanometre repeatability," Nucl. Instrum. Methods Phys. Res. Sect A **616**, 224–228 (2010).
12. O. Hignette, A. K. Freund, and E. Chinchio, "Incoherent x-ray mirror surface metrology," Proc. SPIE **3152**, 188–199 (1997).
13. M. L. Hart, M. Drakopoulos, C. Reinhard, and T. Connolley, "Complete elliptical ring geometry provides energy and instrument calibration for synchrotron-based two-dimensional X-ray diffraction," J. Appl. Cryst. **46**(5), 1249–1260 (2013).
14. J. Filik, A. W. Ashton, P. C. Y. Chang, P. A. Chater, S. J. Day, M. Drakopoulos, M. W. Gerring, M. L. Hart, O. V. Magdysyuk, S. Michalik, A. Smith, C. C. Tang, N. J. Terrill, M. T. Wharmby, and H. Wilhelm, "Processing two-dimensional X-ray diffraction and small-angle scattering data in *DAWN 2*," J. Appl. Cryst. **50**(3), 959–966 (2017).
15. M. Sánchez del Río and R. J. Dejus, "Status of XOP: an x-ray optics software toolkit," Proc. SPIE **5536**, 171–174 (2004).